

Scaling Calibration in Region of Interest Reconstruction with the 1D and 2D ATRACT Algorithm

Yan Xia · Frank Dennerlein · Sebastian Bauer · Hannes Hofmann ·
Joachim Hornegger · Andreas Maier

Abstract

Purpose Recently, a reconstruction algorithm for region of interest (ROI) imaging in C-arm CT was published, named Approximate Truncation Robust Algorithm for Computed Tomography (ATRACT). Even in the presence of substantial data truncation, the algorithm is able to reconstruct images without the use of explicit extrapolation or prior knowledge. However, the method suffers from a scaling and offset artifact in the reconstruction. Hence, the reconstruction results are not quantitative. It is our goal to reduce the scaling and offset artifact so that Hounsfield unit (HU) values can be used for diagnosis.

Methods In this paper, we investigate two variants of the ATRACT method and present the analytical derivations of these algorithms in the Fourier domain. Then, we propose an empirical correction measure that can be applied to the ATRACT algorithm, to effectively compensate the scaling and offset issue. The proposed method is evaluated on ten clinical datasets in the presence of different degrees of artificial truncation.

Results With the proposed correction approach, we achieved an average relative root mean square error (rRMSE) of 2.81% with respect to non-truncated FDK (Feldkamp, Davis, and

Kress) reconstruction, even for severely truncated data. The rRMSE is reduced to as little as 10% of the image reconstructed without the scaling calibration.

Conclusions The reconstruction results show that ROI reconstruction of high accuracy can be achieved since the scaling and offset artifact is effectively eliminated by the proposed method. With this improvement, the HU values may be used for post-processing operations such as bone or soft tissue segmentation if some tolerance is accepted.

Keywords Region of interest imaging · Dose reduction · Truncation correction · Scaling calibration

Introduction

In three-dimensional (3D) X-ray imaging during an intervention, changes of the examined patient are often restricted to a small part of the field of view (FOV). For example, in neuroradiology, only a tiny device, e.g. an implanted stent or coil, is required to be examined multiple times. This suggests region of interest (ROI) imaging utilizing an X-ray beam collimator to laterally and axially block radiation during the image acquisition, so that only the area of interest is irradiated by X-rays. Although the radiation dose to the patient will be considerably reduced during ROI imaging, the corresponding 3D reconstruction from lateral data truncation poses a challenge to conventional tomographic reconstruction algorithms, e.g. the FDK method [8]. Due to the non-local property of the ramp filter, FDK reconstruction of any point of an object requires the knowledge of the projections away from the point at the same lateral position. This requirement, however, is not satisfied anymore if projection data are laterally truncated. Thus, a noticeable degradation of image quality manifesting as a cupping-like low-frequency artifact will be observed in the reconstruction.

So far various truncation correction methods have been proposed to overcome the effect of the truncation artifact. In

The authors gratefully acknowledge funding by Siemens AG, Healthcare Sector and of the Erlangen Graduate School in Advanced Optical Technologies (SAOT) by the German Research Foundation (DFG) in the framework of the German excellence initiative.

Y. Xia · H. Hofmann · J. Hornegger · A. Maier
Pattern Recognition Lab, Friedrich-Alexander-University Erlangen-Nuremberg, Erlangen, Germany
E-mail: yan.xia@cs.fau.de

Y. Xia · J. Hornegger
Graduate School in Advanced Optical Technologies (SAOT), Friedrich-Alexander-University Erlangen-Nuremberg, Erlangen, Germany

F. Dennerlein · S. Bauer
Healthcare Sector, Siemens AG, Erlangen, Germany

the field, the most commonly used approach is based on a model-driven extrapolation scheme. Such methods include symmetric mirroring of projection images [13], water cylinder fitting [9], square root extrapolation [15], optimization-based extrapolation [11] and scattering signal-based extrapolation [1]. However, these methods are based on heuristic assumptions that may not always accurately approximate the object outside the FOV/ROI.

Another major category of ROI reconstruction methods requires prior knowledge about the reconstructed object but yields an exact reconstruction if some geometrical conditions are satisfied by the imaging configuration. Reconstruction algorithms of this category are based on a combination of a back projection of the first derivative and 1D Hilbert transform in the object domain [2, 6, 12, 14].

Iterative reconstruction can also be a candidate for tackling the interior problem. Related work focus on the use of compressed sensing [19] and total variation [18]. However, iterative methods entail a higher computational load and are often not practically viable.

Recently, a novel method for ROI reconstruction of highly truncated projection data with neither the use of prior knowledge nor any explicit extrapolation has been suggested [3]. This method (ATRACT) is based on a decomposition of the standard ramp filter within FDK into a local and a non-local filtering step, where the local step is a 2D Laplace operator and the non-local step is a 2D Radon-based filtering [3] or 2D convolution-based filtering [4, 5, 17]. Furthermore, the ATRACT method has been investigated in different decompositions, such as in a 1D filtering that is applied per detector row [16]. The ATRACT method can provide satisfactory reconstruction results even in the presence of severe data truncation. However, it suffers from a global scaling and bias issue in the reconstruction so that the measurement can not be quantitative.

In this paper, we investigate two variants of the ATRACT method, namely 1D ATRACT and 2D ATRACT, named after the dimension of the filter kernel. As a first contribution, we analytically derive both algorithms in the Fourier domain. The two variants consist of a local Laplace operator and a low-pass global filter that are consistent to the original ATRACT formulation [3]. The derivation confirms that these variants of ATRACT are mathematically identical to the standard FDK. Moreover, the proposed methods are computationally more efficient than Radon-based ATRACT since we know the Fourier representation of the kernel; implementing the FFT-based convolution is thus more straightforward. Then, as main contribution, we propose an empirical correction scheme being applied on the investigated ATRACT methods to achieve more accurate ROI reconstructions, particularly regarding the offset problem.

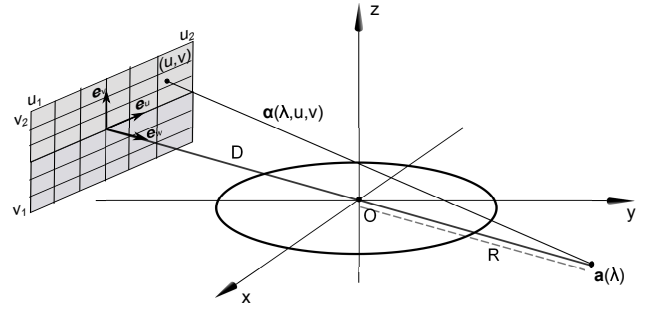


Figure 1 Cone-beam geometry and associated notation: The curve $\mathbf{a}(\lambda) = (R \cos \lambda, R \sin \lambda, 0)$ describes the trajectory of the X-ray source, with the iso-center patient distance R and the rotation angle λ . The planar detector is parallel to the unit vectors $\mathbf{e}_u(\lambda)$ and $\mathbf{e}_v(\lambda)$ and at distance D from the source. $\mathbf{e}_w(\lambda)$ is the detector normal. The function $g(\lambda, u, v)$ is used to describe the projection data at the point (u, v) acquired at angle λ .

Materials and Methods

1D Convolution-based ATRACT

In this section, we describe the first variant of the ATRACT method that comes with a two-step row-wise filtering. We refer to this method as 1D ATRACT below. Let us denote the object density function $f(\mathbf{x})$ with $\mathbf{x} = (x, y, z)$ and the trajectory of the source $\mathbf{a}(\lambda) = (R \cos \lambda, R \sin \lambda, 0)$. Focusing on the circular cone-beam (CB) imaging geometry with a flat-panel detector shown in Fig. 1, the 2D projection at the rotation angle λ obtained for all possible unit vectors $\boldsymbol{\alpha}$ with can be written as

$$g(\lambda, u, v) = \int_0^\infty f(\mathbf{a}(\lambda) + t\boldsymbol{\alpha}(\lambda, u, v)) dt, \quad (1)$$

with

$$\boldsymbol{\alpha}(\lambda, u, v) = \frac{1}{\sqrt{u^2 + v^2 + D^2}} (ue_u + ve_v - D\mathbf{e}_w), \quad (2)$$

where \mathbf{e}_w is the unit vector orthogonal to the detector plane and pointing toward the source, and \mathbf{e}_u and \mathbf{e}_v are orthogonal unit vectors pointing in the direction along which u and v are measured.

To derive 1D ATRACT, the standard ramp filter is decomposed into the 1D Laplace filter and a 1D convolution-based filter. The application of the standard 1D ramp filtering in the Fourier domain can be written as follows:

$$g_F(\lambda, u, v) = \mathcal{F}_1^{-1} \{ \mathcal{F}_1 \{ g_1 \}(\lambda, \omega_u, v) |\omega_u| \}, \quad (3)$$

where \mathcal{F}_1 and \mathcal{F}_1^{-1} denote the 1D Fourier transform and 1D inverse Fourier transform with respect to u , and $g_1(\lambda, u, v)$ denotes the pre-weighted projection data for the cone-beam short scan. $|\omega_u|$ is the ramp kernel in the Fourier domain, which can be further decomposed as follows

$$\begin{aligned}
|\omega_u| &= \omega_u \operatorname{sgn}(\omega_u) = i2\pi\omega_u \frac{1}{i2\pi} \operatorname{sgn}(\omega_u) \\
&= (i2\pi\omega_u)^2 \left(-\frac{1}{4\pi^2} \frac{\operatorname{sgn}(\omega_u)}{\omega_u} \right). \quad (4)
\end{aligned}$$

Substituting Eqn. (4) into (3), we can obtain an alternative expression of ramp filtering:

$$g_F(\lambda, u, v) = \mathcal{F}_1^{-1} \left\{ \left(-\frac{1}{4\pi^2} \frac{\operatorname{sgn}(\omega_u)}{\omega_u} \right) \cdot (i2\pi\omega_u)^2 \cdot \mathcal{F}_1 \{g_1\}(\lambda, \omega_u, v) \right\}. \quad (5)$$

It is well-known that multiplication in the Fourier domain corresponds to convolution in the spatial domain. We can thus transform Eqn. (5) into the spatial domain with a convolution of two other terms, as the inverse 1D Fourier transform of $(i2\pi\omega_u)^2 \mathcal{F}_1 \{g_1\}$ gives $\partial^2 g_1 / \partial u^2$ (see Appendix for the derivation), i.e., the 1D Laplace operation with respect to u , and the inverse 1D Fourier transform of $-\operatorname{sgn}(\omega_u) / \omega_u$, which yields the 1D residual kernel $\ln|u|$.

Using the same pre-scaling scheme and 3D cone-beam backprojection as FDK, the 1D ATRACT algorithm consists of the following four steps:

- *Step 1:* Cosine- and Parker-like weighting of projection data to obtain pre-scaled projection data $g_1(\lambda, u, v)$:

$$g_1(\lambda, u, v) = \frac{Dm(\lambda, u)}{\sqrt{D^2 + u^2 + v^2}} g(\lambda, u, v), \quad (6)$$

where D denotes the source-detector distance, $m(\lambda, u)$ is the Parker weight to compensate for data redundancy.

- *Step 2:* 1D Laplace filtering to obtain projection data $g_2(\lambda, u, v)$:

$$g_2(\lambda, u, v) = \frac{\partial^2}{\partial u^2} g_1(\lambda, u, v). \quad (7)$$

- *Step 3:* 1D convolution-based filtering to get the filtered data $g_F(\lambda, u, v)$

$$g_F(\lambda, u, v) = -\frac{1}{4\pi^2} \int_{-\infty}^{\infty} g_2(\lambda, u - u', v) \ln|u'| du'. \quad (8)$$

- *Step 4:* 3D cone-beam backprojection with a weighting function of object-focal point distance to get the estimated object function $f(\mathbf{x})$:

$$f^{(ATRACT)}(\mathbf{x}) = \int_{\lambda_1}^{\lambda_2} \frac{RD}{[R - \mathbf{x} \cdot \mathbf{e}_w(\lambda)]^2} g_F(\lambda, u, v) d\lambda, \quad (9)$$

where $[\lambda_1, \lambda_2]$ is the short scan angular range.

The benefits of considering this two-step filtering instead of the standard ramp filtering are:

1) The first filtering step (1D Laplace operation) is a pure local operation to the projection data and can thus be computed accurately even if projection data are truncated. Errors will only be introduced at the border of the FOV since the outer values are unknown. In the numerical implementation, we remove these incorrect values (singularities) by setting the values at border pixels to be 0. In standard FDK on the other hand, such removal is not straightforward and the non-local ramp filtering will perturb the whole projections in the presence of data truncation.

2) After the Laplace operation, the values of $g_2(\lambda, u, v)$ are much closer distributed around 0 than the values of g_1 . This implies that the extrapolation with constant 0 for the missing data in the second-order derivative domain that was implicitly performed, is a good approximation prior to applying the residual global filtering.

3) Although the residual filtering is a non-local operation, it is less sensitive to data inconsistencies due to its low-pass character. Consequently, even though no explicit extrapolation is used during the filtering steps in ATRACT, the filtered result $g_F(\lambda, u, v)$ will not contain a noticeable cupping-like artificial structure at the borders of lateral truncation compared to that of the FDK method.

2D Convolution-based ATRACT

Since 2D filtering can be performed for all detector elements simultaneously, it could reduce outliers that may be caused by individual 1D processing of the detector lines. In this section we investigate a 2D version of the ATRACT method that has potential to increase the image quality of ROI reconstruction [4, 17]. Below, we present the analytical derivation of this algorithm in the Fourier domain using a similar approach as we did in 1D ATRACT. Using Cartesian coordinates in the frequency plane, the 2D version of the ramp filtering in the Fourier domain can be expressed as:

$$g_F(\lambda, u, v) = \mathcal{F}_2^{-1} \{ \mathcal{F}_2 \{g_1\}(\lambda, \omega_u, \omega_v) |\omega_u| \}, \quad (10)$$

where \mathcal{F}_2 is the 2D Fourier transform and \mathcal{F}_2^{-1} denotes its inversion.

We can decompose the ramp kernel into

$$|\omega_u| = \frac{-1}{4\pi^2} \frac{|\omega_u|}{(\omega_u)^2 + (\omega_v)^2} \left((i2\pi\omega_u)^2 + (i2\pi\omega_v)^2 \right). \quad (11)$$

Inserting Eqn. (11) into Eqn. (10) yields

$$g_F(\lambda, u, v) = \mathcal{F}_2^{-1} \left\{ \frac{-1}{4\pi^2} \frac{|\omega_u|}{\omega_u^2 + \omega_v^2} \left((i2\pi\omega_u)^2 + (i2\pi\omega_v)^2 \right) \cdot \mathcal{F}_2 \{g_1\}(\lambda, \omega_u, \omega_v) \right\}. \quad (12)$$

Analogously, we can transform Eqn. (12) into the spatial domain with a convolution, where the inverse 2D Fourier transform of $\left((i2\pi\omega_u)^2 + (i2\pi\omega_v)^2 \right) \mathcal{F}_2 \{g_1\}(\lambda, \omega_u, \omega_v)$ gives $(\partial^2/\partial u^2 + \partial^2/\partial v^2)g_1(\lambda, u, v)$, and the inverse 2D Fourier transform of $|\omega_u|/(\omega_u^2 + \omega_v^2)$ yields

$$\begin{aligned} h_{2D}(u, v) &= \int_{-\infty}^{\infty} \int_{-\infty}^{\infty} \frac{|\omega_u|}{\omega_u^2 + \omega_v^2} e^{i2\pi(u\omega_u + v\omega_v)} d\omega_u d\omega_v \\ &= \int_{-\infty}^{\infty} e^{-u|\omega_v|} e^{i2\pi v\omega_v} d\omega_v \\ &= \frac{|v|}{u^2 + v^2}, \end{aligned} \quad (13)$$

where $h_{2D}(u, v)$ is the spatial representation of the 2D convolution kernel.

Now we obtain the 2D ATRACT algorithm by substituting the filtering steps 2 and 3 in 1D ATRACT as follows:

- *Step 2:* 2D Laplace filtering to obtain projection data $g_2(\lambda, u, v)$:

$$g_2(\lambda, u, v) = \left(\frac{\partial^2}{\partial u^2} + \frac{\partial^2}{\partial v^2} \right) g_1(\lambda, u, v). \quad (14)$$

- *Step 3:* 2D convolution-based filtering to get the filtered data $g_F(\lambda, u, v)$

$$g_F(\lambda, u, v) = \frac{-1}{4\pi^2} \int_{-\infty}^{\infty} \int_{-\infty}^{\infty} g_2(\lambda, u - u', v - v') \frac{|v'|}{u'^2 + v'^2} du' dv'. \quad (15)$$

Note that there is a singularity in the filter kernel at $(0, 0)$. In the numerical implementations, we address this by computing the mean value of its neighboring positions, i.e., for $u = \pm 0.1, v = \pm 0.1$. The 2D ATRACT method is intrinsically robust to data truncation due to its two-step filtering. Meanwhile, it has the potential to further increase the image quality compared to the 1D ATRACT approach due to its 2D processing.

Scaling and Offset Artifact in ATRACT

In the ATRACT algorithm, we remove the singularities at the borders of lateral data truncation after Laplace filtering. This causes a loss of the information on the thickness of the object. The following residual filtering of truncated projections will result in an offset or bias with respect to the FDK filtering of non-truncated projections. For visualization, we manually performed a correction of this bias in the final reconstructed volume for each dataset previously.

In this paper, we investigate an automatic correction scheme for this problem. Note that throughout this paper we use the term “given scenario” to denote the same acquisition geometry and application scenario, i.e. a patient head scan in our case. Depending on the information available, one of the two procedures proposed below is used to deal with this problem.

Min-Max Scaling. If no prior knowledge is available in the given scenario, then a simple min-max scaling method is utilized to the backprojected results, to roughly align the total intensity values to a reasonable range (-1024 ~ 3072 HU). The min-max scaling method is applied on the reconstructed volume $f(\mathbf{x})$ and is used to avoid clamping the over-saturated values caused by an incorrect offset in the last stage of the imaging pipeline. However, note that it would introduce an additional scaling problem and thus should only be used when offset correction (as introduced in the following paragraph) cannot be applied.

$$f(\mathbf{x})^{\min_max} = \frac{(f(\mathbf{x}) - f_{min})}{(f_{max} - f_{min})} \cdot 4096 - 1024, \quad (16)$$

where

$$f_{min} = \min(f(\mathbf{x}_i)) \quad \text{and} \quad f_{max} = \max(f(\mathbf{x}_i))$$

The min-max scaling can only enable a linear relationship, rather than an exact HU value match, between the FDK reconstruction from a full FOV scan and ATRACT-based ROI reconstruction.

Offset Correction. Now we introduce our correction approach that can be applied on the filtered data $g_F(\lambda, u, v)$, to more accurately compensate the scaling/offset problem generated by ATRACT. The scheme is based on the following correction model:

$$g_F^{\text{corrected}}(\lambda, u, v) = g_F(\lambda, u, v) + \epsilon(\lambda), \quad (17)$$

and

$$\begin{aligned} \epsilon(\lambda) &= A \cdot \sum_{u_1}^{u_2} \sum_{v_1}^{v_2} g(\lambda, u, v) \Delta u \Delta v + B \\ &\quad + C \cdot (u_2 - u_1) \cdot (v_2 - v_1) \end{aligned} \quad (18)$$

where $g_F(\lambda, u, v)$ and $g_F^{\text{corrected}}(\lambda, u, v)$ denote the filtered projections by ATRACT without and with correction, ϵ is the

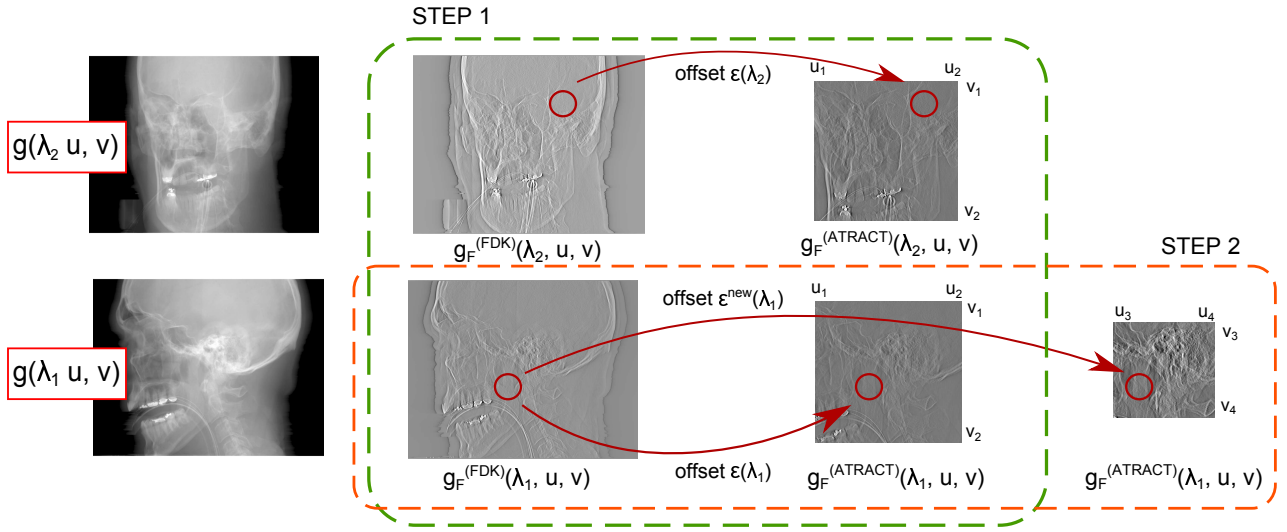


Figure 2 Illustration of the calibration procedure using full FOV scan data (data courtesy of St. Luke’s Episcopal Hospital, Houston, TX, USA). Step 1 involves determining the attenuation-related parameters A and B_1 using two projections from different views $g(\lambda_1, u, v)$ and $g(\lambda_2, u, v)$ by comparing the difference between the mean values of selected ROIs (marked as red circles) in FDK and ATRACT filtered projections. With determined A and B_1 , a different truncation size was chosen (i.e., $(u_4 - u_3) \cdot (v_4 - v_3)$) in the same angulation λ_1 , to calculate the size-related parameters B_2 and C using Eqn. (20).

projection-dependent offset and Δu , Δv are spacings in u and v direction. In principle, the offset problem discussed before can also be regarded as a loss of the information on the object support. We empirically found that this information is related to the attenuation summation $\sum_{u_1}^{u_2} \sum_{v_1}^{v_2} g(\lambda, u, v)$ and truncation size $(u_2 - u_1) \cdot (v_2 - v_1)$. We can approximately recover this information, i.e. $\epsilon(\lambda)$, by setting the attenuation related linear parameters A and B and truncation size related parameter C .

Let us now detail the estimation of the parameters in Eqn. (18). These parameters are calibrated by measuring the differences (offsets) between the ATRACT filtered truncated projections and the ramp filtered non-truncated projection (FDK). In particular, the estimation divides into two steps (also see Fig. 2 for illustration):

- *Step 1*: First we computed the parameter A and an intermediate parameter B_1 using two different truncated projections with the same truncation size:

$$\begin{cases} B_1 + A \cdot \sum_{u_1}^{u_2} \sum_{v_1}^{v_2} g(\lambda_1, u, v) \Delta u \Delta v = \epsilon(\lambda_1) \\ B_1 + A \cdot \sum_{u_1}^{u_2} \sum_{v_1}^{v_2} g(\lambda_2, u, v) \Delta u \Delta v = \epsilon(\lambda_2) \end{cases} \quad (19)$$

- *Step 2*: With A and B_1 determined in Step 1), we estimate another two parameters B_2 and C from projection data with a different truncation size:

$$\begin{cases} B_1 + A \cdot \sum_{u_1}^{u_2} \sum_{v_1}^{v_2} g(\lambda_1, u, v) \Delta u \Delta v + B_2 \\ \quad + C \cdot (u_2 - u_1) \cdot (v_2 - v_1) = \epsilon(\lambda_1) \\ B_1 + A \cdot \sum_{u_3}^{u_4} \sum_{v_3}^{v_4} g(\lambda_1, u, v) \Delta u \Delta v + B_2 \\ \quad + C \cdot (u_4 - u_3) \cdot (v_4 - v_3) = \epsilon^{\text{new}}(\lambda_1) \end{cases} \quad (20)$$

where B_1 and B_2 are two additive parameters. Note that in Eqn. (18), they are combined into a single parameter ($B = B_1 + B_2$).

In practice, the determination of calibration parameters depends on the specific clinical scenario: 1) If a prior full scan projections are available and the ROI scans are used as follow-up scan to re-examine the patient, we can calibrate the parameters using Eqn. (18). 2) If no prior full scan is available and only truncated data are acquired, we use the parameters that were pre-set in an initial calibration step using another patient full scan in the same application scenario. In this work, we focus on the latter case which is more generic, and the application scenario is a patient head scan.

Experimental Setup

The proposed correction scheme was validated and evaluated on ten clinical datasets of patient heads (data courtesy of St. Luke’s Episcopal Hospital, Houston, TX, USA and Rush University Medical Center, Chicago, IL, USA). All datasets were acquired on a C-arm CT system (Artis Zee, Siemens AG, Forchheim, Germany). All scans contain 496 projection images 1240×960 pixels with a resolution of 0.308 mm/pixel and were acquired on a 200° short-scan circular trajectory.

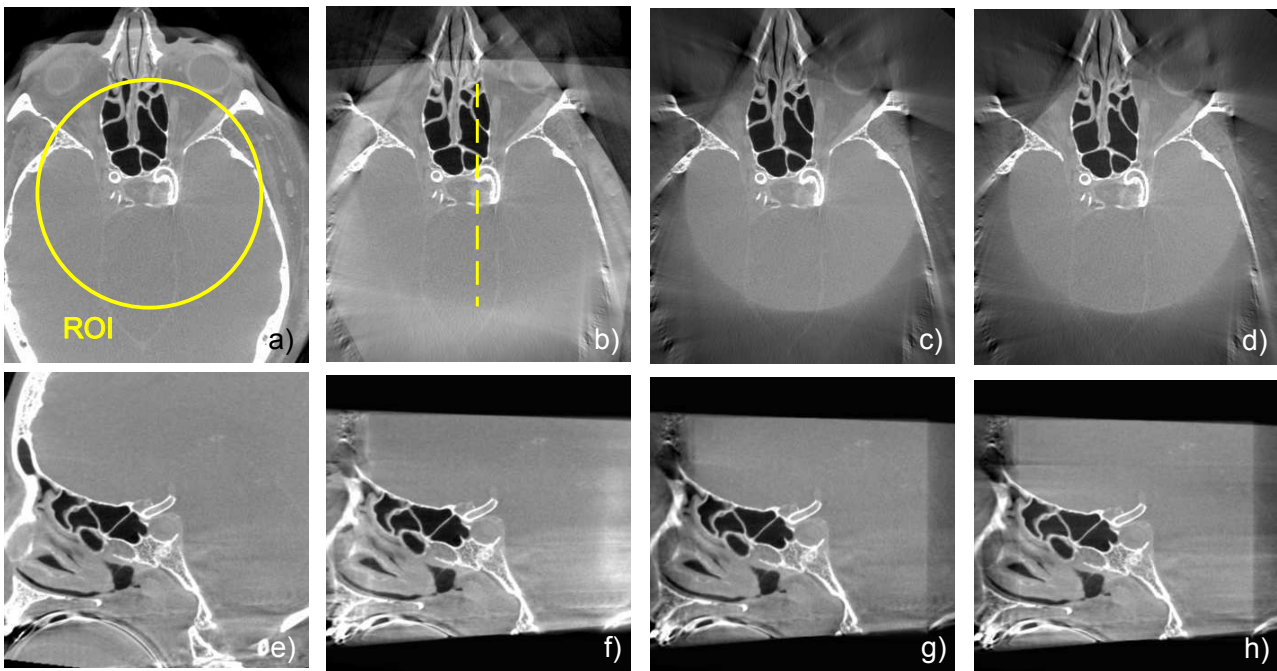


Figure 4 Reconstruction results of the clinical dataset I (data courtesy of St. Luke’s Episcopal Hospital, Houston, TX, USA), in the grayscale window [-1000 HU, 1000 HU]. From left to right: The gold standard FDK reconstruction from non-truncated data, the water cylinder extrapolation-based ROI reconstruction, the 2D ATRACT-based ROI reconstruction with offset correction, the 1D ATRACT-based ROI reconstruction with offset correction. The diameter of the FOV in the truncated data is 104 mm and is marked as the yellow circle.

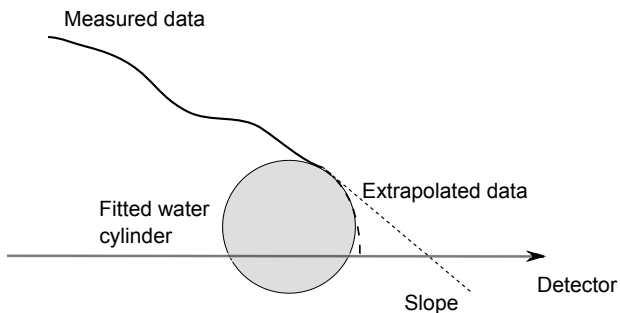


Figure 3 Illustration of water cylinder extrapolation process for truncated data.

Four experimental setups were considered. In Setup 1, no collimation was applied, yielding non-truncated projection data. In Setup 2, 3 and 4, the datasets were virtually collimated (by setting the values outside the FOV to be 0) to three different levels (FOV diameter: 104 mm, 72 mm and 40 mm), so that only the small FOV was kept in the projection data.

All clinical data were reconstructed onto a Cartesian grid ($512 \times 512 \times 350$) with an isotropic voxel size of 0.4 mm^3 . The standard FDK reconstruction of Setup 1 on non-truncated projections was used as the reference for quantitative evaluation in each clinical case. The truncated datasets were reconstructed using the 1D ATRACT and 2D ATRACT algorithm, with both the min-max scaling and the offset correction. The quantitative evaluation for the ten clinical datasets was carried out by using two image quality metrics: 1) the

relative root mean squared error (rRMSE), calculated by the RMSE value divided by the volume intensity range of the reference and 2) the correlation coefficient (CC). We also investigated the performance of a well-known water cylinder extrapolation method [9] and compare it to our newly proposed method quantitatively. As illustrated in Fig. 3, this extrapolation scheme empirically estimates the missing data as a partial cylindrical water object, to provide the transition between measured data and data outside the FOV to be smooth and differentiable.

In the numerical implementation, the Laplace operation was computed using the finite difference method with either a 3×1 kernel (1D Laplace) or a 3×3 kernel (2D Laplace) and thus filtering can be efficiently performed in the spatial domain. The ATRACT residual filtering was performed using FFT in the Fourier domain. To avoid singularities in the central values of the 1D and 2D convolution kernels, we estimated the central values by computing the mean value at ($u = \pm 0.1, v = \pm 0.1$) in 2D ATRACT and $u = \pm 0.1$ in 1D ATRACT. Note that in all evaluations the parameters A , B and C were determined only once using one single reference dataset (the non-truncated projections of clinical dataset I), with $A = -3.68 \cdot 10^{-7}$, $B = 1.78$, and $C = -6.76 \cdot 10^{-7}$ in 2D ATRACT and with $A = -9.03 \cdot 10^{-8}$, $B = 1.25$ and $C = 8.48 \cdot 10^{-7}$ in 1D ATRACT.

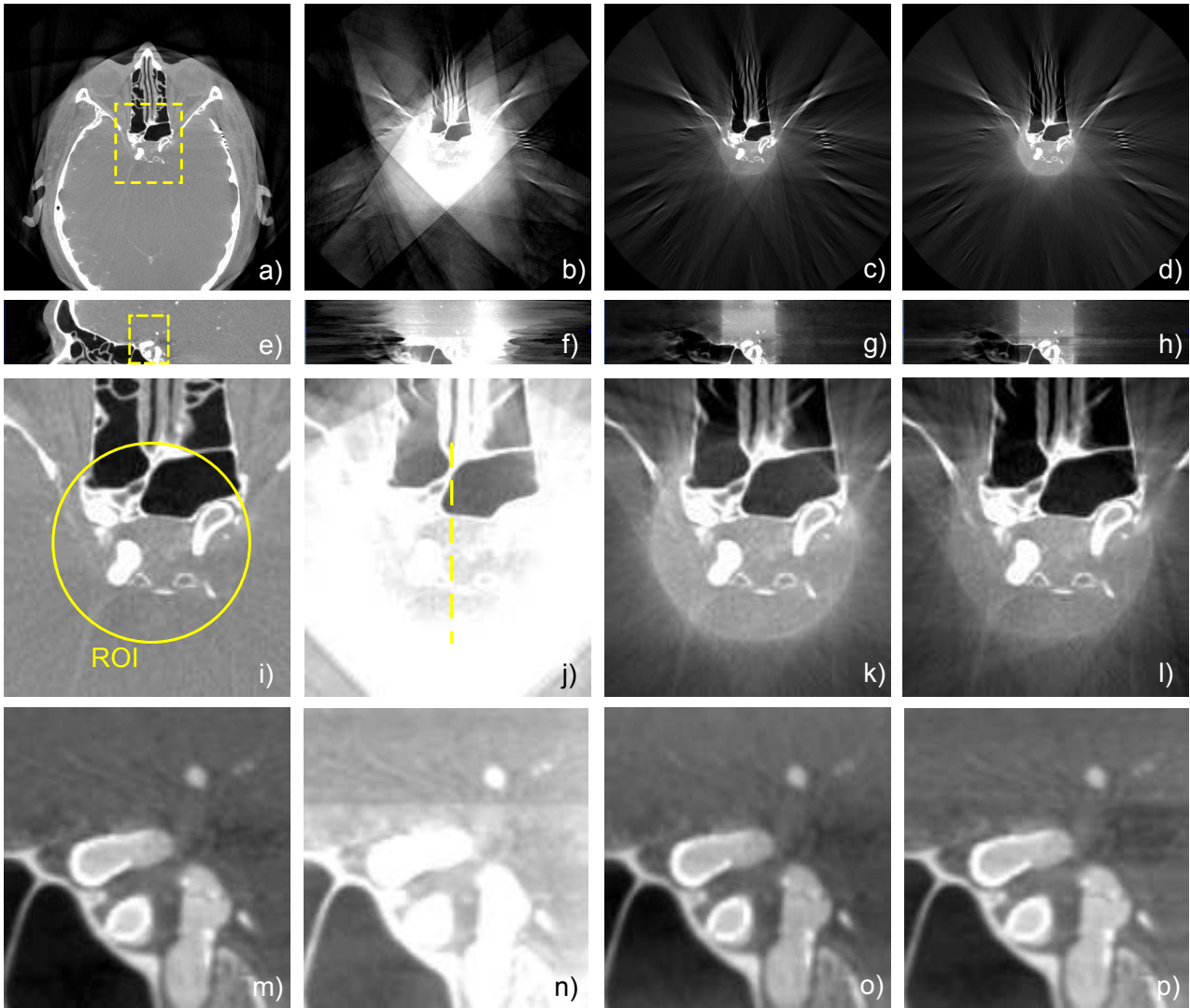


Figure 5 Reconstruction results of the clinical dataset VI (data courtesy of St. Luke’s Episcopal Hospital, Houston, TX, USA), in the grayscale window [-1000 HU, 1000 HU]. From left to right: The gold standard FDK reconstruction from non-truncated data, the water cylinder extrapolation-based ROI reconstruction, the 2D ATRACT-based ROI reconstruction with offset correction, the 1D ATRACT-based ROI reconstruction with offset correction. The third and fourth rows (display window [-1000 HU, 2000 HU]) are zoomed images of the dashed rectangular areas in the first two rows. The diameter of the FOV in the truncated data is 40 mm and is marked as the yellow circle.

Results

The reconstruction results of the clinical dataset I with the FOV of 104 mm and dataset VI with FOV of 40 mm, restored by corrected 1D/2D ATRACT as well as water cylinder extrapolation, are presented in Fig. 4 and Fig. 5. Corresponding line profiles are shown in Fig. 6 and 7.

For the reconstruction results of the 104 mm FOV, no substantial difference within the FOV is observed between all three ROI reconstructions and the reference FDK reconstruction from non-truncated data. The line profiles (line position shown as the yellow dashed line), from which no significant deviation was seen compared to the reference, also confirm this visual observation. However, with increasing degree of truncation, the water cylinder extrapolation suffers

from truncation-induced cupping artifacts at the boundaries of the FOV while corrected 1D and 2D ATRACT still maintain high image quality (see Fig. 7).

Fig. 8 shows a homogeneous area of the reconstruction by corrected 2D ATRACT from clinical dataset IV, for the truncated data with a FOV diameter of 104 mm and 72 mm, respectively. It can be observed that the proposed correction scheme not only effectively reduces truncation artifacts and nicely restores the structural information, but also yields a highly comparable intensity magnitude as non-truncated FDK due to the automatic scaling/offset correction, even though the calibration parameters were determined by clinical dataset I.

Fig. 9 and 10 show volume renderings of implanted micro devices from the standard FDK reconstruction from non-

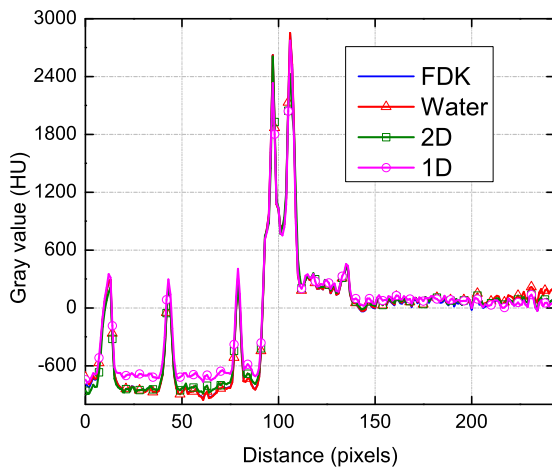


Figure 6 The central line profile (line position marked as the yellow dashed line in Fig. 4, i.e. medium truncation case) along each reconstruction. Note that all three algorithms achieve comparable results to the reference.

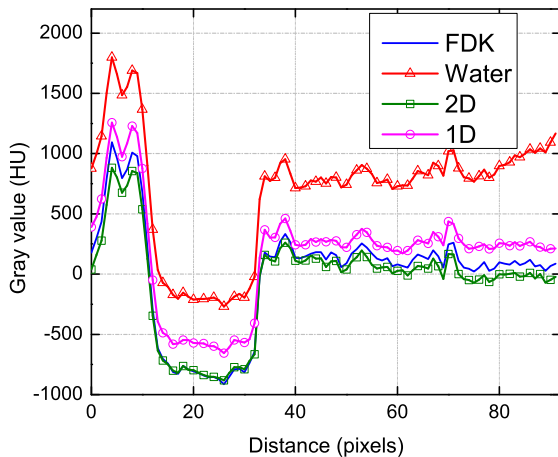


Figure 7 The central line profile (line position marked as the yellow dashed line in Fig. 5, i.e. severe truncation case) along each reconstruction. Note that truncation-introduced cupping artifact and bias appear in the water cylinder extrapolation for this severe truncation case while 2D and 1D ATRACT still yield reconstructions of high quality.

truncated data and the new ATRACT reconstruction from truncated data. In Fig. 9, the truncated FOV is $\sim 30\%$ of the full FOV, which means that a dose reduction of $\sim 70\%$ could be achieved in this case. In Fig. 10, the projection data were highly truncated, yielding a possible dose reduction of $\sim 91\%$. Note that in both truncation cases the visualization quality of the neurological stent or coil is almost identical to the one reconstructed from non-truncated data entailing a substantially larger X-ray exposure.

The quantitative evaluation of the reconstructions of all ten clinical datasets by 1D ATRACT, 2D ATRACT and water cylinder extrapolation are summarized in Table 1, Table 2 and Table 3, respectively. The mean value and standard deviation of rRMSE as well as CC are also presented as column

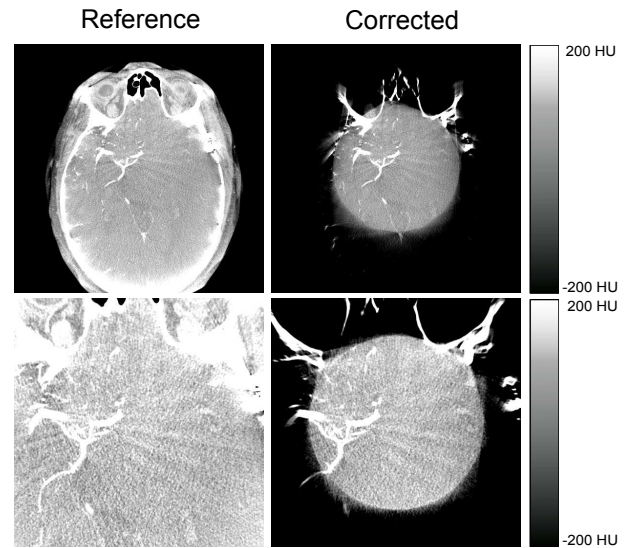


Figure 8 Homogeneous area of the reconstructions of the clinical dataset IV (data courtesy of St. Luke's Episcopal Hospital, Houston, TX, USA), in a compressed display window $[-200 \text{ HU}, 200 \text{ HU}]$. Left column: the gold standard FDK reconstruction, right column: the 2D ATRACT ROI reconstruction by the corrected 2D ATRACT. The first and second row are reconstructed from truncated FOV of 104 mm and 72 mm, respectively.

graph in Fig. 11, 12 and 13. We found that even for severely truncated data (FOV of 40 mm), the corrected 1D ATRACT method achieved a mean rRMSE of 3.27% compared to a mean rRMSE of 15.3% for its uncorrected version. For corrected 2D ATRACT, the average rRMSE was 2.81%. This confirms that the proposed scaling correction performs well in all evaluated datasets, even though the correction parameters were estimated from one dataset and applied to the others. Note that since the correlation coefficient is free of the scaling and bias problem in the reconstruction, no significant differences can be observed for these values between the corrected ATRACT and the uncorrected one.

Also note that there is no observable difference between the image quality of reconstructions from truncated data with the FOV diameter of 104 mm and of 72 mm for 1D/2D ATRACT approach. We found that the water cylinder extrapolation performs nicely for the truncated FOV of 104 mm. Both rRMSE and CC values are comparable to the ATRACT methods. But when the truncation becomes more severe, e.g. with the FOV diameters of 72 mm and 40 mm, it is not able to accurately approximate the missing data and thus results in a lower image quality: A mean rRMSE of 5.14% for the 72 mm FOV and 11.9% for the 40 mm FOV.

Discussion and Conclusion

Typically, 3D C-arm CT scans cause a considerable amount of effective dose up to 2.7 mSv for a low-contrast scan of the patient's head [7]. ROI imaging, which deploys a collimator

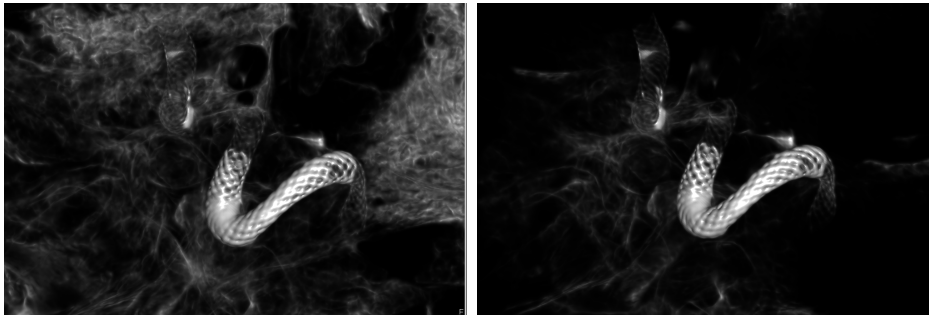


Figure 9 3D volume rendering of an implanted neurological stent from the FDK reconstruction of the full FOV scan (left) and from ATRACT-based ROI reconstruction of truncated FOV scan (right) (data courtesy of St. Luke’s Episcopal Hospital, Houston, TX, USA). Note that image quality from truncated FOV data is visually comparable to that from the full FOV scan while the former enables considerable dose reduction compared to the latter.

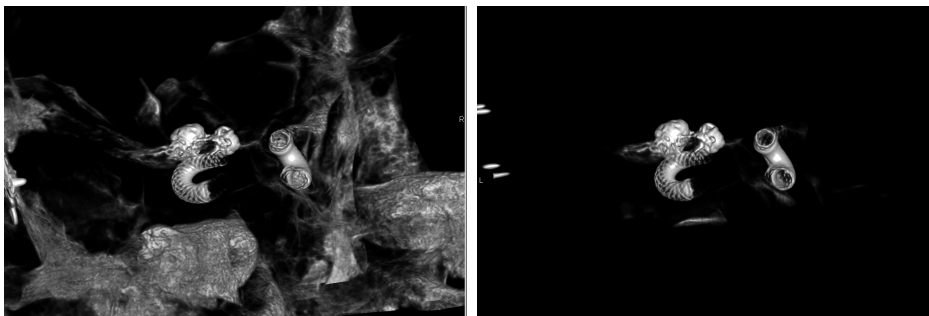


Figure 10 3D volume rendering of two implanted stents and a coil from the FDK reconstruction of the full FOV scan (left) and from ATRACT-based ROI reconstruction of severely truncated FOV scan (right) (data courtesy of St. Luke’s Episcopal Hospital, Houston, TX, USA). The potential dose reduction of 91% can be achieved in this severe truncation.

Table 1 Quantitative evaluation of the reconstructions of the ten patient head datasets using the corrected 1D ATRACT algorithm.

FOV	Metrics	Data I	Data II	Data III	Data IV	Data V	Data VI	Data VII	Data VIII	Data IX	Data X
104 mm	CC	0.98	0.97	0.97	0.97	0.92	0.96	0.95	0.96	0.96	0.96
	rRMSE (%)	1.28	2.39	1.36	2.29	2.09	1.60	1.62	3.24	2.31	2.66
72 mm	CC	0.98	0.97	0.97	0.97	0.92	0.97	0.97	0.96	0.96	0.96
	rRMSE (%)	1.08	1.99	2.06	2.31	2.44	1.28	1.59	2.13	1.96	2.71
40 mm	CC	0.98	0.94	0.98	0.95	0.90	0.98	0.92	0.84	0.91	0.94
	rRMSE (%)	2.70	2.16	4.11	1.64	7.34	4.32	1.31	2.44	3.18	3.57

Table 2 Quantitative evaluation of the reconstructions of the ten patient head datasets using the corrected 2D ATRACT algorithm

FOV	Metrics	Data I	Data II	Data III	Data IV	Data V	Data VI	Data VII	Data VIII	Data IX	Data X
104 mm	CC	0.99	0.98	0.97	0.98	0.96	0.98	0.97	0.96	0.95	0.97
	rRMSE (%)	0.92	1.72	1.55	2.10	1.36	1.48	1.47	3.67	3.99	2.37
72 mm	CC	0.98	0.99	0.97	0.99	0.99	0.99	0.97	0.96	0.95	0.98
	rRMSE (%)	0.92	1.49	2.54	1.99	2.04	1.53	1.61	2.04	4.43	1.89
40 mm	CC	0.98	0.97	0.98	0.96	0.94	0.98	0.96	0.89	0.91	0.98
	rRMSE (%)	1.22	2.13	3.95	4.71	3.55	2.43	1.79	3.15	3.31	1.88

Table 3 Quantitative evaluation of the reconstructions of the ten patient head datasets by means of the water cylinder extrapolation.

FOV	Metrics	Data I	Data II	Data III	Data IV	Data V	Data VI	Data VII	Data VIII	Data IX	Data X
104 mm	CC	0.97	0.98	0.98	0.98	0.92	0.97	0.96	0.98	0.95	0.97
	rRMSE (%)	1.15	2.13	1.62	1.78	2.39	2.01	0.72	2.70	2.62	2.41
72 mm	CC	0.96	0.95	0.97	0.95	0.96	0.98	0.92	0.93	0.92	0.95
	rRMSE (%)	3.15	6.38	5.78	5.66	8.08	2.88	2.22	4.90	6.15	6.25
40 mm	CC	0.90	0.85	0.97	0.88	0.93	0.95	0.92	0.86	0.87	0.93
	rRMSE (%)	9.13	9.38	7.78	18.6	16.5	9.12	4.62	15.7	16.0	12.6

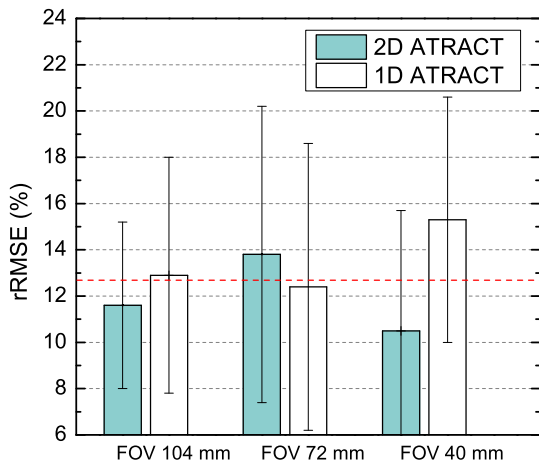


Figure 11 Mean values and standard deviations of the rRMSE from the reconstructions of three FOVs using the uncorrected 1D/2D ATRACT algorithms.

to shield X-rays outside of the diagnostic ROI, will dramatically reduce radiation dose to the patient. The amount of dose savings is approximately proportional to the truncated FOV.

However, the resulting truncation poses a challenge to traditional reconstruction algorithms. In this article, we investigated two variants of an existing truncation correction method (ATRACT) and presented an empirical scaling correction that can be applied to these methods. The advantages of the proposed method are addressed by the following aspects: 1) As opposed to the algorithms reported in [2, 12, 14], the proposed method relies very little prior knowledge and is not restricted to a limited family of data sets. This enables practicality of the algorithms in most interventional use cases. 2) Compared to the iterative methods in [18] and [19], the new methods adopt the filtered back-projection scheme and can be directly applied in a clinically used scanner at low computational cost. For instance, the total computation time of iterative methods is proportional to $I \cdot O(N^3) + I \cdot O(N^4)$, where I is the number of iterations (assume that projection dimension size, projection number and volume size are equal to N). In contrast, the standard FBP scheme only requires the one step back-projection of the filtered projections with a complexity of $O(N^4)$. 3) Explicit extrapolation methods [1, 9, 11, 13, 15] are interventional preferred since they are computationally efficient and are able to estimate the missing data heuristically without the requirement of prior knowledge. They are, however, difficult to apply to severe truncations that are encountered in ROI scans, as shown in Fig. 5.

Fig. 11 and 12 showed that with the proposed offset correction, ATRACT is able to effectively reduce the rRMSE to as little as 2.06%, compared to the one without correction (11.2%). Unlike an atlas-based linear correction that require a large patient database [10], the newly proposed calibration

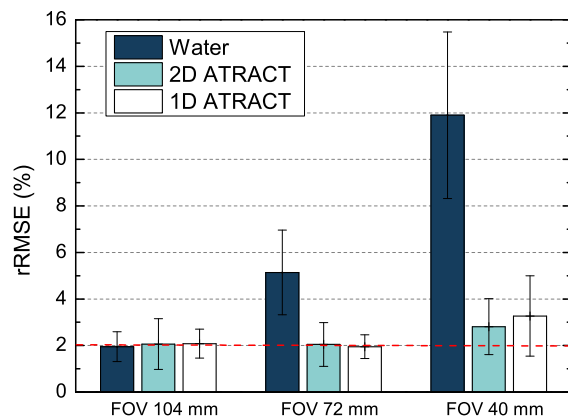


Figure 12 Mean values and standard deviations of the rRMSE from the reconstructions of three FOVs using the corrected 1D/2D ATRACT as well as water cylinder extrapolation algorithms.

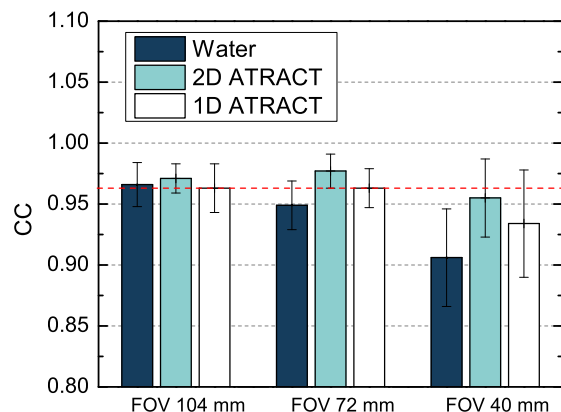


Figure 13 Mean values and standard deviations of the CC (correlation coefficient) from the reconstructions of three FOVs using the corrected 1D/2D ATRACT as well as water cylinder extrapolation algorithms.

measure is only performed once with one dataset and the determined parameters can be factory pre-set for a given organ program at the scanner. The corrected intensity range can also enable the application of post-processing algorithms that rely on values of final reconstructed volume to work properly. A potential limitation of this study is its restriction to patient head datasets. Differences between the anatomy are likely to result in variations in projection correction parameters. Future work involves the validation in larger studies.

Appendix

Assume the 1D Fourier transform of $g_1(\lambda, u, v)$ with respect to u is $\mathcal{F}_1\{g_1\}(\lambda, \omega_u, v)$, then we can obtain

$$g_1(\lambda, u, v) = \int_0^{\infty} \mathcal{F}_1\{g_1\}(\lambda, \omega_u, v) e^{i2\pi\omega_u u} d\omega_u \quad (21)$$

Applying the second-order derivative to both side of the equation above yields

$$\begin{aligned} \frac{\partial}{\partial u^2} g_1(\lambda, u, v) &= \frac{\partial}{\partial u^2} \int_0^{\infty} \mathcal{F}_1\{g_1\}(\lambda, \omega_u, v) e^{i2\pi\omega_u u} d\omega_u \\ &= \int_0^{\infty} \mathcal{F}_1\{g_1\}(\lambda, \omega_u, v) \frac{\partial}{\partial u^2} e^{i2\pi\omega_u u} d\omega_u \\ &= \int_0^{\infty} \left[\mathcal{F}_1\{g_1\}(\lambda, \omega_u, v) (2\pi i \omega_u)^2 \right] e^{i2\pi\omega_u u} d\omega_u \end{aligned} \quad (22)$$

Then, the inverse Fourier transform of $(i2\pi\omega_u)^2 \mathcal{F}_1\{g_1\}$ is equivalent to $\partial^2 g_1 / \partial u^2$ has been shown.

Conflicts of interest Yan Xia receives financial support from Siemens AG, Healthcare Sector and Erlangen Graduate School in Advanced Optical Technologies (SAOT). Frank Dennerlein and Sebastian Bauer are employees of Siemens AG, Healthcare Sector, Germany.

Disclaimer The concepts and information presented in this paper are based on research and are not commercially available.

References

- Bier, B., Maier, A., Hofmann, H., Schwemmer, C., Xia, Y., Struffert, T., Hornegger, J.: Truncation correction for VOI C-arm CT using scattered radiation. In: Proc. SPIE, vol. 8668, p. 86682F9 (2013)
- Defrise, M., Noo, F., Clackdoyle, R., Kudo, H.: Truncated Hilbert transform and image reconstruction from limited tomographic data. *Inverse Probl.* **22**(3), 1037–1053 (2006)
- Dennerlein, F.: Cone-beam ROI reconstruction using the Laplace operator. In: Proc. Fully 3D 2011, pp. 80–83 (2011)
- Dennerlein, F., Maier, A.: Region-of-interest reconstruction on medical C-arms with the ATRACT algorithm. In: Proc. SPIE, p. 83131B (2012)
- Dennerlein, F., Maier, A.: Approximate truncation robust computed tomography - ATRACT. *Physics in Medicine and Biology* **58**, 6133–6148 (2013)
- Dennerlein, F., Noo, F., Schoendube, H., Hornegger, J., Lauritsch, G.: A factorization approach for cone-beam reconstruction on a circular short-scan. *IEEE Trans. Med. Imag.* **27**(7), 887–896 (2006)
- Fährig, R., Dixon, R., Payne, T., Morin, R.L., Ganguly, A., Strobel, N.: Dose and image quality for cone-beam C-arm CT system. *Med. Phys.* **33**(12), 4541–4550 (2006)
- Feldkamp, L.A., Davis, L.C., Kress, J.W.: Practical cone beam algorithm. *J. Opt. Soc. Am.* **1**, 612–619 (1984)
- Hsieh, J., Chao, E., Thibault, J., Grekowicz, B., Horst, A., McOlash, S., Myers, T.J.: A novel reconstruction algorithm to extend the CT scan field-of-view. *Med. Phys.* **31**(9), 2385–2391 (2004)
- Maier, A., Jiang, Z., Jordan, J., Riess, C., Hofmann, H., Hornegger, J.: Atlas-Based Linear Volume-of-Interest (ABL-VOI) Image Correction. In: Proc. SPIE, vol. 8668, p. 86682D (2013)
- Maier, A., Scholz, B., Dennerlein, F.: Optimization-based Extrapolation for Truncation Correction. In: 2nd CT Meeting, pp. 390–394 (2012)
- Noo, F., Clackdoyle, R., Pack, J.D.: A Two-step Hilbert Transform Method for 2D Image Reconstruction. *Phys. Med. Biol.* **49**(17), 3903–3923 (2004)
- Ohnesorge, B., Flohr, T., Schwarz, K., Heiken, J.P., Bae, J.P.: Efficient correction for CT image artifacts caused by objects extending outside the scan field of view. *Med. Phys.* **27**(1), 39–46 (2000)
- Pan, X., Zhou, Y., Xia, D.: Image reconstruction in peripheral and central region-of-interest and data redundancy. *Med. Phys.* **32**(3), 673–684 (2005)
- Sourbelle, K., Kachelriess, M., Kalender, W.A.: Reconstruction from truncated projections in CT using adaptive detruncation. *Eur. Radiol.* **15**(5), 1008–1014 (2005)
- Xia, Y., Maier, A., Dennerlein, F., Hofmann, H., Mueller, K., Hornegger, J.: Reconstruction from Truncated Projections in Cone-beam CT using an Efficient 1D Filtering. In: Proc. SPIE, vol. 8668, p. 86681C (2013)
- Xia, Y., Maier, A., Dennerlein, F., Hofmann, H.G., Hornegger, J.: Efficient 2D filtering for cone-beam VOI reconstruction. In: Proc. IEEE NSS-MIC, pp. 2415–2420 (2012)
- Yang, J., Yu, H., Jiang, M., Wang, G.: High-order total variation minimization for interior tomography. *Inverse probl.* **26**(3), ID: 035,013 (2010)
- Yu, H., Wang, G.: Compressed sensing based interior tomography. *Phys. Med. Biol.* **54**(9), 2791–2805 (2009)